

Unsteady aerodynamics computation and investigation of magnus effect on computed trajectory of spinning projectile from subsonic to supersonic speeds

F.A. Chughtai 

Department of Mechanical & Aerospace Engineering
Institute of Avionics & Aeronautics
Air University
Islamabad, Pakistan
faheem.chughtai@outlook.com

J. Masud

Department of Mechanical & Aerospace Engineering, Institute of Avionics & Aeronautics
Air University
Islamabad, Pakistan

S. Akhtar

School of Engineering Technology
National University of Technology
Islamabad, Pakistan

ABSTRACT

This paper describes the extensive numerical investigation carried out on a 203-mm spin-stabilised projectile to study the effects of Magnus force at high angles of attack on the stability and flight-trajectory parameters, for further validation and incorporation in a 6-DOF trajectory solver for flight-stability analysis. Magnus force typically influences the course of flight by causing the projectile to drift from its intended path in addition to generation of inbuilt dynamic instabilities in pitch and yaw orientation and is a function of AoA and spin rate. This study is a consolidation of the authors' previous research on the same caliber projectile but with time-accurate analysis. It has been found that typically, the Magnus force and moment calculation requires time-accurate Navier Stokes equations to be solved numerically for accurate prediction^(1,2). Hence, to complete the extraction of static and dynamic coefficients derivatives, unstructured time-accurate CFD analysis on multiple configurations,

ranging from subsonic to supersonic Mach regimes, has been evaluated using Large Eddy Simulation (LES) and found to be suitable for capturing the desired effects. However, the LES simulation requires non-dimensional wall distance (y^+) of the order of 0.5–1, with $LES_IQ > 75\%$ thus, is computationally-intensive. In addition, to cover the entire flight envelope from Charge 1 (249 m/s) to Charge 7 (595 m/s), at spin rate from 500 rad/s to 750 rad/s, 30 cases have been evaluated to generate the time-accurate coefficient library for integration with 6-DOF solver analysis. The results obtained have been compared with the available experimental data and found to be in reasonable agreement. The results of 6-DOF solver, incorporating the extracted coefficients, were compared with firing-table results, which further validated the computational methodology. This study provides an insight on how opposite flow interacts with the attached boundary layer due to spin rate and generates a turbulent interacting flow with variation in vortical structures for Q-Criterion vortex-flow visualization.

Keywords: Magnus effect; spinning projectile; LES analysis; 6DOF trajectory; FFT; precession; nutation

NOMENCLATURE

\hat{C}	reference length
Cd	coefficient of drag $\{D / (1/2\rho V^2 S_{ref})\}$
Cl	coefficient of lift $\{L / (1/2\rho V^2 S_{ref})\}$
Cl_p	roll damping coefficient $\{2V_T(\partial Cl / \partial \rho) / \hat{C}\}$
Cm	coefficient of pitching moment $\{M_x / (1/2\rho V^2 S_{ref} \cdot \hat{C})\}$
Cn_ρ	Magnus moment coefficient $\{\partial Cn / \partial \rho\}$
Cy_ρ	Magnus force coefficient $\{\partial Cy / \partial \rho\}$
Cn_β	yaw stiffness $\{\partial Cn / \partial \beta\}$
Cy	side force coefficient $\{Y / (1/2\rho V^2 S_{ref})\}$
Cy_β	side force due to side slip angle $\{\partial Cy / \partial \beta\}$
St	Strouhal number (f.U/D)
Y^+	non dimensional wall distance
WT	wind tunnel

Greek Symbol

α, β	Angle of attack and side-slip angle (rad)
ψ	Yaw Angle (rad)
p	Role Rate (rad/sec)
ρ	Air density at sea-level, 1.225 kg/m ³

Subscript

$(\cdot)_{\alpha, \beta, p}$ First derivative $\partial(\cdot)$ wrt α, β or p

Abbreviations

AoA	Angle of Attack α (rad)
AoS	Side Slip Angle β (rad)

<i>CFD</i>	Computational Fluid Dynamics
<i>CFD SS</i>	CFD Steady State
<i>CFF</i>	Custom Field Function
<i>DOF</i>	Degree of Freedom
FFT	Fast Fourier Transform
<i>LES</i>	Large Eddy Simulation Turbulence Model
<i>LES_IQ</i>	LES Index Quality
<i>LNS</i>	Limited Numerical Scale Model
<i>M</i>	Mach number
<i>MV</i>	Muzzle Velocity
<i>RANS</i>	Reynolds Average Navier Stokes
<i>RBD</i>	Rigid Body Dynamics
<i>SA</i>	One equation Spalarat-Allamaras turbulence model
Sgs	Subgrid-scale model
<i>TKE</i>	Turbulence Kinetic Energy
WALE	Wall-Adapted Local Eddy-Viscosity

1.0 INTRODUCTION

Flow over streamlined bodies and aero vehicles has been experimented on extensively over the past few decades to analyse the flow pattern and surface pressure distribution. The forces and moments that a projectile or an aero vehicle encounters during flight needs detailed analysis for optimal design calculations. The boundary-layer (BL) in spinning projectiles has a specific swirling pattern. This directional flow pattern within the BL on interaction with free stream flow at certain AoA, defines the magnitude of the Magnus forces and moments. The lateral force alters the course of projectile trajectory once launched at certain elevation from the intended path. All parameters, which affect the BL thickness and flow characteristics, affect the Magnus force. These may include the surface fineness, AoA, Mach number, Reynolds number, spin rate or projectile geometry. The work already done provides a detailed database of Magnus force calculation, whether it be the wind-tunnel-mounted projectiles testing^(3,4); free-flight experiments, which were extensively conducted by U.S. Army Ballistic Research Laboratory⁽⁵⁻⁹⁾; empirical modeling^(10,11); or the numerical analysis^(1,2,12-14). How the Magnus force and moment varies with Mach number, AoA, AoS and spin rate from subsonic to supersonic speeds, cross-sectional variation in pressure distribution with respect to AoA, visualization of vortex core ripples due to interaction of opposite flows, resonant frequency oscillations and FFT-based spectral analysis of nutation and precession frequencies dependencies on Magnus force/moment, are yet to be elaborated and are the scope of this paper.

The projectile chosen for this study is a M106 203-mm (8-inch) spin-stabilised projectile. This large-caliber projectile is designed for HE fragmentation, smoke screen and for limited-yield, tactical nuclear munitions as well (M110 Howitzer and M115 Howitzer capable of delivering 203-mm W33 nuclear shells⁽¹⁵⁾). The model geometry is the same as used in the authors' previous study⁽¹⁶⁾. Since the generation of a static and dynamics derivatives coefficient library is essential for accurate trajectory and flight-stability simulation using 6-DOF equations of motion, proven methodologies for precise calculation of aerodynamics coefficients were evaluated. Empirical datasets, experimental and wind-tunnel-extracted results, have inherent challenges, including high experimental cost and limitation of not being able to capture the entire spectrum of pressure and force-induced dynamics. On the other hand,

numerical analysis has proved to be accurate, cost effective and a viable option, especially for aerodynamics analysis. In particular, for flight stability and trajectory analysis, coupled CFD/RBD as well as uncoupled schemes have been extensively evaluated. Advantage of coupled analysis is a real-time feedback loop system, which allows the effect of changing flight parameters to be incorporated directly into numerical scheme, allowing perturbation analysis to be simulated effectively. The disadvantage is that a coupled system is computationally very intensive and requires high-end processing. An uncoupled scheme involves extraction of aerodynamics data via CFD over the entire flight envelop and further integration with 6-DOF motion solver as a lookup table. An uncoupled scheme gives more flexibility for system-dynamics analysis and is computationally economical. The surveyed literature, including empirical methods, coupled unsteady and uncoupled steady state, and transient analysis of spinning projectile are tabulated in Table 1.

The present study is a comprehensive presentation of time-accurate extraction of static and dynamic derivatives of the 203-mm spinning projectile from Charge 1 (Mach 0.7) to Charge 7 (Mach 1.7). Previous RANS studies^(16,21) showed that steady state computation does accurately predict the static derivatives, and trajectory analysis showed reasonable agreement with experimental results. However, Magnus force and moment effects cannot be captured accurately, and these effects needs to be incorporated especially for stability analysis. More recent research by U.S. Army Research Laboratory (ARL)⁽¹⁾ found that time-accurate, advance-turbulence modelling (e.g., hybrid RANS or Large Eddy Simulation - LES) was more effective in capturing the Magnus effect and in determination of dynamic derivatives including roll/pitch damping, Magnus force and moment coefficients.

2.0 NUMERICAL APPROACH

2.1 Grid generation

The geometry and CAD model of the 203-mm projectile understudy is generated using Creo Parametric. The model was imported to Pointwise, a CFD meshing tool, in which surface and volume meshes were developed. Since for LES turbulence modeling, non-dimensional wall distance is required to be of the order of 1 or <1 ($y^+ \leq 1$) to accurately resolve the boundary layer, hence, surface meshing and boundary-layer resolution was selected keeping in view the computational requirement. The projectile spin rate for each charge (1–7) was calculated from barrel-twist rate and exit velocity, which gives the non-dimensional spin rate ($\frac{\omega d}{2V}$) of 0.125, with spin rate ranging from 308–594 rad/sec and corresponding exit velocity from 233–534m/sec, respectively.

The procedure for LES analysis followed in the present study includes detailed flow analysis using steady RANS, based on which the assessment for required mesh resolution for LES analysis was carried out. Another RANS simulation on the new LES mesh was performed for further mesh adaptation at the near wall region and assessment for required temporal resolution. Synthetic turbulence needs to be superimposed on the mean flow of computational domain to introduce instantaneous velocities and to disturb the steady state pattern, for LES analysis to achieve faster statistically average-able state. For the current scale resolving simulation, precursor $k-\epsilon$ turbulence RANS model was used based on the previous study⁽¹⁶⁾. In the present analysis, main emphasis remained on a well resolved near wall region rather than resolving eddies in the mean flow. The Magnus effect so generated is directly affected by wall shearing differential with respect to the AoA and spin rate and

Table 1
Recent published research on spinning projectile magnus effect estimation

First Author	Year	Projectile	Mesh Type	Solution Type		Turbulence Model	CFD results Validation against Experimental Data	CFD / Empirical Solver
				Steady State	Transient			
Leszek Baranowski ⁽¹⁰⁾	2013	155mm, ogive nose	-	-	-	-	-	Arrow Tech PRODAS
Mostafa Khalil ⁽¹¹⁾	2009	155mm M107 projectile	-	-	-	-	-	SPINNER-98
Sidra I. Silton ⁽¹⁾	2011	0.50 cal	Unstructured	✓	✓	<ul style="list-style-type: none"> • RANS - cubic k ε model • LES - Smagorinsky model 	✓	CFD++
Jubaraj Sahu ⁽¹³⁾	2009	155 mm, ogive cylinder boattail	Hybrid unstructured 5 Mn cell Y+ 1	-	Coupled CFD / RBD (transonic speed)	¥	✓	CFD++
Jubaraj Sahu ⁽¹²⁾	2011	155 mm, ogive nose	Unstructured 5 Mn cell Y+ 1	-	Coupled CFD / RBD (subsonic - supersonic speed)	¥	✓	CFD++
Tomi Honkanen	2012	7.62 mm bullet	Unstructured 2 Mn cell Y+ 1	✓	✓	¥	✓	<ul style="list-style-type: none"> • OpenFOAM 1.7.0 • ANSYS fluent 12.1

**Table 1
Continued**

First Author	Year	Projectile	Mesh Type	Solution Type		Turbulence Model	CFD results Validation against Experimental Data	CFD / Empirical Solver
				Steady State	Transient			
James DeSpirito ⁽²⁾	2006	25-mm sub-caliber training projectile (conical ogive)	Unstructured 1.9 Mn cell $Y+ < 1$	-	✓	✓ Realizable2 eqn k-ε model ✓ 3 eqn k-ε-R ✓ DES	✓	CFD++ PRODAS
D. Klatt ⁽¹⁴⁾	2013	30mm, generic tangential-ogive-cylinder type projectile	Unstructured hexahedral grids 2.9 Mn cells $Y+ 1$	✓	-	RANS (k- ω model)	✓	ANSYS fluent V13
M.E. Wessam ⁽¹⁹⁾	2015	155mm M107 projectile	Unstructured hexahedral 0.34 Mn cells $Y+ 60$	✓		Spalart-Allmaras model	✓	ANSYS fluent 14.5
Habib ⁽²⁰⁾ Belaidouni	2016	122mm projectile	3 mn cells	✓		✓ Realizable2 eqn k-ε model ✓ 4 eqn SST model	✓	• Ansys fluent 14 • Gambit 2.4

¥ - Information not available

RBD - Rigid Body Dynamics, LNS - Hybrid RANS/LES, DES - Detached Eddy Simulation

needs to be mimicked accurately. Hence Sub Grid Scale WALE model with $y(+) \leq 1$ has been applied, as discussed later.

The meshing was carried out keeping in view the incompressible to supersonic nature of the flight regime, with sufficiently high Reynolds number ($3.2 - 7.3 \times 10^6$) corresponding to the highly turbulent nature of the flow. Furthermore, CFL condition or courant number is kept 1 for subsonic and 0.5 or even 0.05 for initial stabilization of the numerical scheme in transonic and supersonic cases. Four x meshes for steady-state analysis were analysed based on RANS turbulent modeling (SA & k- ϵ) in the previous study⁽¹⁶⁾ and two x meshes analysed for the current transient analysis as tabulated in Table 2 below. Volume-grid spacing of $1.6 \mu\text{m}$ is kept for the first 20 layers in volume extrusion, with a growth rate of 1.15 to achieve the final mesh for analysis. $y(+) \leq 1$ is kept for the selected LES turbulent model to accurately resolve the boundary-layer for capturing the Magnus effect with max resolution of Turbulent Kinetic Energy. An estimate of integral length scale l_0 (at which turbulent kinetic energy (TKE) peaks) was made based on precursor RANS, with the aim to resolve 70–80% TKE. 1st cell height of $1.6 \mu\text{m}$ was selected with 3–5 cells across l_0 . The anisotropic tetrahedral extruded layers (T-Rex cells) algorithm is used for sharp edges for surface meshing as well as for volume extrusion of boundary layer into an unstructured block. The T-Rex algorithm generates refined mesh in near wall region by extruding regular layers of tetrahedral from the boundaries. The mesh adapts to convex/concave regions and colliding extrusion fronts thereby generating high-quality cells. Three separate blocks were made, with a highly dense inner mesh block, to accurately capture shock effect and near-wall disturbance/eddies. An outer less-dense, structured rectangular block was used capturing the wake. Pictorial views of the mesh are depicted from Figs. 1–4.

2.2 Grid optimization

Two meshes, with sufficiently fine surface mesh and boundary-layer extrusion with T-Rex cell (anisotropic tetrahedral extrusion), were developed to study grid independence (mesh 5 and 6, respectively) and were validated against available experimental data of the drag coefficient from Mach 0.7 to Mach 1.6 at zero AoA and Magnus force coefficient for Mach 0.7. Both meshes were found to predict with reasonable accuracy (<5% deviation from experimental drag-coefficient calculation⁽⁸⁾), hence, no further mesh was analysed. Being computationally economical, mesh #5 was selected for subsequent analysis. It has been found that steady-state (SS) analysis with k- ϵ turbulence model predicts the drag coefficient in close agreement with experimental data as compared to time-accurate analysis with LES at subsonic speed. However, at transonic and supersonic speed, time-accurate LES models provide much more accurate predictions. The Table 2 shows various meshes used for the current series of analyses. Drag coefficient, predicted with SS analysis (mesh #4)⁽¹⁶⁾, transient (mesh #5) and experimental testing at zero AoA, is compared below (Fig. 5).

Comparison of the drag coefficient (Cd) and Magnus force coefficient ($Cy_{\rho\alpha}$), with selected mesh as per grid independence investigation extracted from experimental^(7,8) and numerical analysis (SS and transient - LES), is shown in Figs. 5 and 6, respectively. Notably, the experimental Magnus force coefficient, as referred to in Ref 7, was calculated based on reversed interpolation with modified point-mass trajectory model, while adjusting the form factor to match the experimental range-firing impact point and time-of-flight data. Robert. F. Lieske's⁽⁷⁾ experimental calculation of Magnus force coefficient ($cy_{\rho\alpha} = 0.38$) was found to accurately predict the Magnus effect at subsonic mach speeds. Keeping in view the limitation of available experimental results, subsonic comparison of numerical analysis versus experimental

Table 2
Mesh used for grid independence study

Surface Mesh		Propagation Parameters			Volume Mesh		Outer Sphere		Inner Sphere		
Mesh No	$\Delta S M$	Surface Cell Count	Max Layers	Full Layers	Growth Rate	$\Delta S M$	Volume Cells Count	Radii M	$\Delta S M$	Radii M	$\Delta S M$
Steady-State Analysis											
Mesh 1	0.01	7391	10	1	1.2	0.0003	0.99Mn	10	1	-	-
Mesh 2	0.008	16700	10	1	1.2	0.0003	1.94Mn	10	0.8	-	-
Mesh 3	0.006	26000	10	1	1.2	0.0003	3.39Mn	10	0.8	-	-
Mesh 4	0.006	26000	10	1	1.2	0.0003	4.44Mn	10	0.8	1	0.03
Unsteady Analysis											
Mesh 5	0.004	103,944	20	2	1.15	1.6e-06	21.89Mn	10	0.8	1.5	0.02
Mesh 6	0.003	198,456	20	2	1.2	1.6e-06	40.8Mn	10	0.8	1.5	0.02

M – Meters,
Mn - Million.

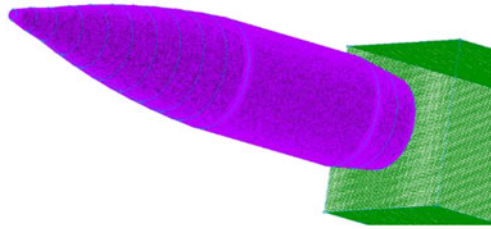


Figure 1. Surface mesh with structured wake block.

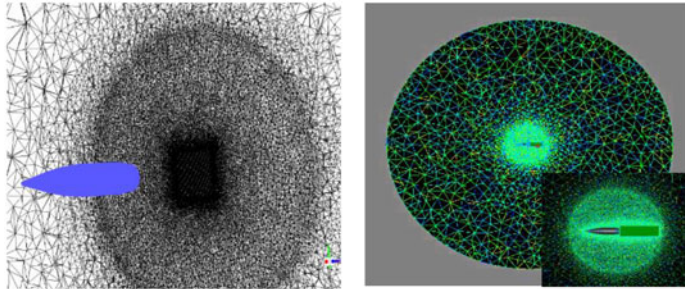


Figure 2. Volume mesh with unstructured dense inner circle.

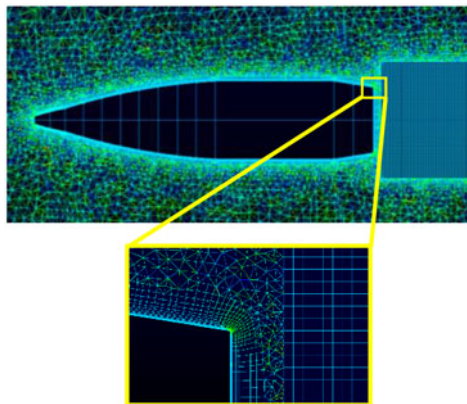


Figure 3. Boundary layer enlarged view.

data of $cy\rho_\alpha$ is considered for the current study and found to be in reasonable agreement for validation of the numerical scheme under study, as shown in Fig. 6.

2.3 Time independence study

The spatial and time domains are both interrelated in an accurate capturing of pressure and viscous effects. The time step and mesh fineness needs to be small enough for precise capturing of small eddies, generated as a byproduct of complex turbulent flow. Balance needs to be maintained, both for mesh fineness and time stepping, for the problem to be computationally economical. Since transient analysis is required to capture the Magnus effects, LES model that is selected requires Y^+ value of the order of 1. For such a fine boundary layer

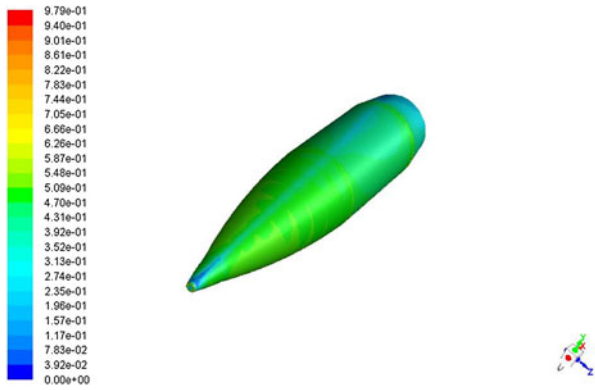


Figure 4. Y Plus distribution on projectile surface at Mach 0.7.

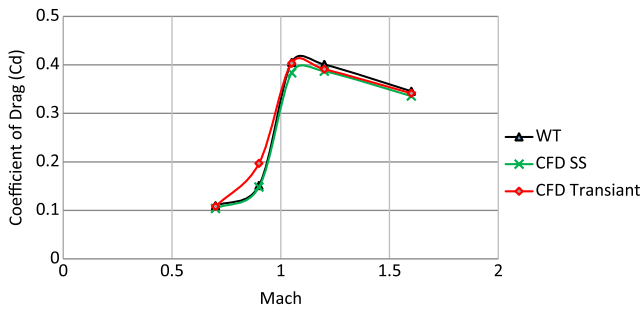


Figure 5. Drag coefficient comparison- validation of computational model.

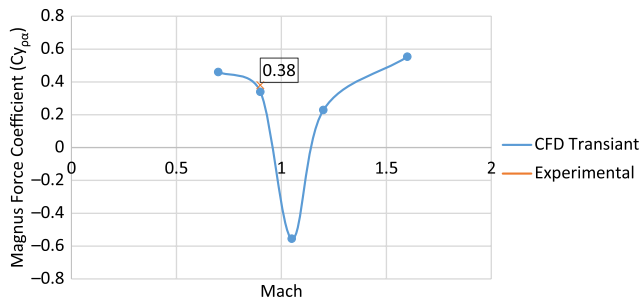


Figure 6. Magnus force ($C_{y_{p\alpha}}$) comparison - validation of computational model.

($\Delta S = 1.6e-6m$), the time step needs to be adjusted accordingly. As per CFL criteria, the ideal time step for the courant number of 1 in the entire Mach scheme is selected. Four time steps have been analysed at Mach 0.7 and 500 rad/sec rotational spin rate at 0° AoA, as plotted below (Fig. 7) and compared with the experimental results⁽⁸⁾. It has been found that drag coefficient C_d remains reasonable accurate for all the time steps that have been compared and is found to be in best agreement at a time step of $O e^{-5}$. However, for CFL criteria of courant number of < 1 and Y^+ of the order of 1 (for LES transient analysis), the time step needs to be

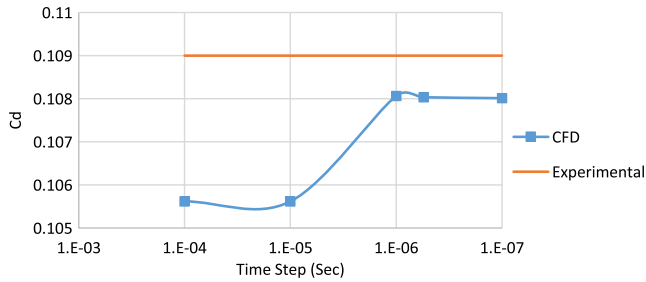


Figure 7. Drag coefficient variation with time step refinement at M 0.7, spin rate 500rad/s.

refined to the order of e^{-6} . Hence, in addition to Cd, $Cy\rho_\alpha$ validation has also been considered for validation of solution model. $Cy\rho_\alpha$ is calculated with time step of $O e^{-6}$ and found to be in agreement with the experimental results (Fig. 6).

3.0 SOLUTION TECHNIQUE

Since spinning projectile at small AoA (approximately 12° , typically encountered during projectile motion) for compressible flight regime undergoes flow wrapping over the projectile surface, which generates large energetic swirling eddies behind the boat-tail (aft). This complex swirling flow in the form of large vortices, carrying major kinetic and viscous flow energies, affects the upstream flow-generating fluctuations/vibrations in the projectile attitude. The effect of small structural is modeled by using sub-grid scale turbulence model for small-scale motions. Hence, time-accurate Large Eddy Simulation Model (LES) is used for the current analysis, which solves the large-scale fluctuating motions and models the smaller ones. Wall-Adapted Local Eddy-Viscosity (WALE) model as a subgrid-scale (SGS) model (with C_{wale} 0.325 and Energy Prandtl Number 0.85, the inherent default values) along with energy equation model has been used. WALE is known to have overcome some of the known deficiencies of the Smagorinsky model, as it inhibits production of eddy-viscosity in laminar flows, thus, effectively reproducing laminar to turbulent transition. No slip moving wall boundary condition was imposed to simulate the spin. The solution methodology adopted includes implicit formulation with Roe-FDS Flux type, using Node-Based Green-Gauss as a spatial discretization gradient method, with second order upwind flow discretization. The transient formulation equation was kept second order implicit, with higher order relaxation of flow variables only. As already discussed, courant number (CFL criteria) was kept in the range 1–0.5 as required for optimal performance of the selected model. The solution was run for 40 iteration/time steps, which effectively converged to the desired convergence limits (Oe^{-4}). The solution for each transient case was initialised with an already converged steady-state analysis after imposing synthetic turbulence, which helps in achieving more stable and faster numerical computation.

A few indicators needs to be monitored during post processing to estimate the quality of the SGS resolution. The resolved part of TKE can be estimated using Custom Field Functions (CFFs). However, the calculated quantities are sampled by averaging from instantaneous values at different time steps, for use in CFFs. The resolved spectrum at the projectile wall and in the entire domain is plotted in Fig. 8(a) and (b), respectively. It can be clearly seen that 99.8% of TKE is resolved near the wall region whereas for the internal domain the resolved

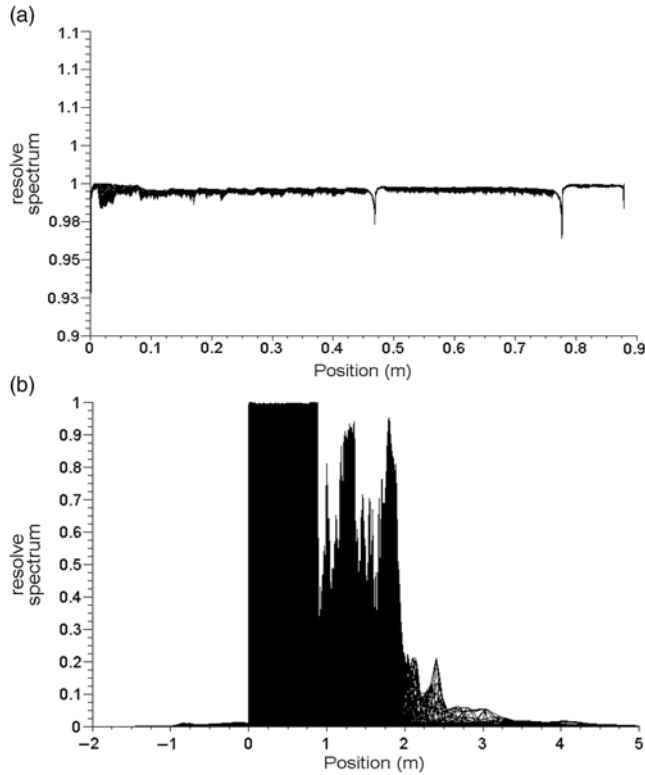


Figure 8. (a): Resolved spectrum – projectile surface. (b): Resolved spectrum - computational domain.

spectrum is 83%. This is sufficient to provide the desired accuracy. The CFF for resolved and modelled turbulent kinetic energies has been evaluated as follows:

$$\text{Resolved}_k = \frac{\left((rmse_{x_{velocity}})^2 + (rmse_{y_{velocity}})^2 + (rmse_{z_{velocity}})^2 \right)}{2} \quad \dots (1)$$

$$K_{sgs} = \frac{sgs_{viscosity_{turbulence}}}{(density \times 0.2 \times \sqrt[3]{cell_{volume}})^2} \quad \dots (2)$$

$$\text{Resolved}_{\text{Spectrum}} = \frac{\text{Resolved}_k}{\text{Resolved}_k + K_{sgs}} \quad \dots (3)$$

Another important parameter to be for LES, to ensure appropriate spectral and temporal resolution, is LES_IQ. It defines the LES calculations based on sub grid scale (SGS) model contribution and numerical discretization errors as a function of grid resolution. The LES index quality criteria as proposed by I.B. Celik⁽¹⁷⁾, has been tested on current domain and was found to be 77%, quite close to the suggested verification index by Celik of 80% or above. CFF used for LES_IQ is as follows:

$$\text{LES}_{IQ} = \frac{1}{\left(1 + 0.5 \times \left(\frac{viscosity_{laminar} + sgs_{viscosity_{turbulence}}}{viscosity_{laminar}} \right)^{0.53} \right)} \quad \dots (4)$$

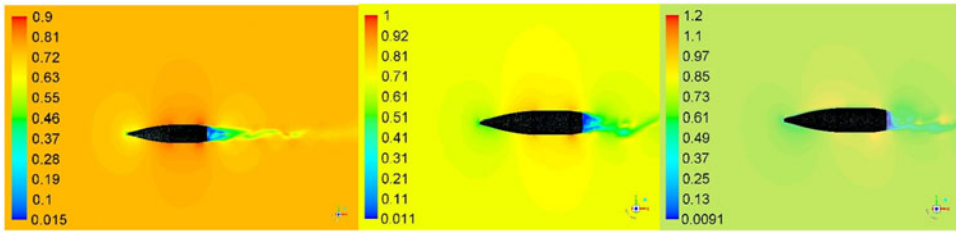


Figure 9. Velocity flow field at M 0.7, AOA 0, 5, 10 (left to right) at time 0.024 sec.

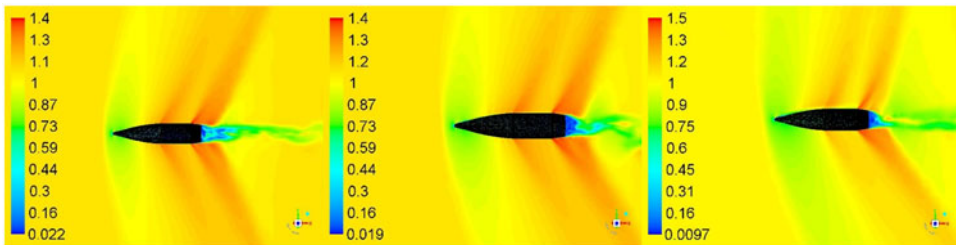


Figure 10. Velocity flow field at M 1.05, AOA 0, 5, 10 (left to right) at time 0.026 sec.

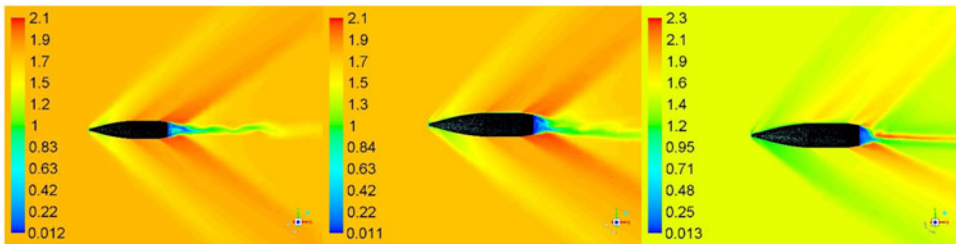


Figure 11. Velocity flow field at M 1.6, AOA 0, 5, 10 (left to right) at time 0.024 sec.

4.0 CFD RESULTS

4.1 Flow field

Trajectory simulations of the projectile under study necessitate generation of an aerodynamic coefficients library encompassing the complete flight envelop. Apropos, 30 cases were simulated from Mach 0.7–1.6 at 0, 5 and 10 degs AoA and at 500–750 rad/s of spin rate, respectively. Each simulation was run to allow the projectile to complete a minimum two rotations (with flow time of approximately 0.024 sec). Keeping in view the periodic boundary condition (with rotation about z-axis simulating the desired spin rate), we observed the quasi steady behavior in the desired coefficient's plots, after one complete rotation (0.012 sec), as depicted in the lift and drag coefficients plots in Fig. 12 below. However, to ensure that the flow field to be fully developed, each case was further run for $T > 0.024$ sec. Mach flow field with cross-sectional planner view at Mach 0.7, 1.05 and 1.6 and at 0, 5 and 10 degs AoA at constant time interval is shown in Figs. 9, 10 and 11, respectively. The velocity

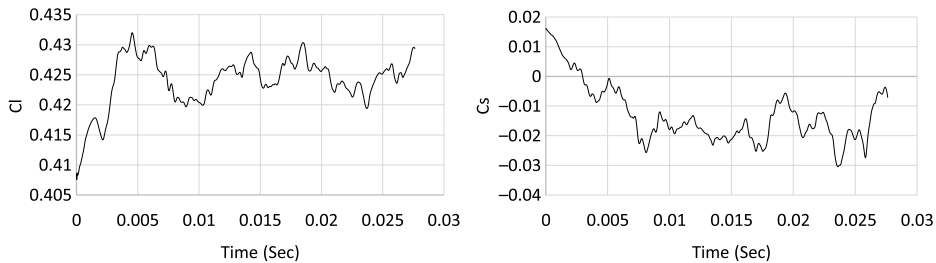


Figure 12. Convergence history of lift and yaw force coefficient (M 1.05, AOA 10 degs, 750 rad/s).

variation/generation of shock wave at supersonic mach speed and fluctuating flow/vortices in wake region at subsonic speed indicates a fully developed flow. The vortex shedding with circulatory flow field (as discussed later in vortex core section) affects the upstream flow (more pronounced in subsonic/transonic flow), and results in pressure/forces fluctuation with respect to time. The effect is visible on time-history plot of Lift (C_l) and Side Force Coefficient (C_s), as plotted in Fig. 12.

A comparison of Mach contour indicates that the flow field depends highly on upstream velocity, geometry of the projectile and AoA. The developed shock wave at Mach 1.6 (Fig. 11) shows a clear decrease in velocity once the flow encounters the shock, whereas at the mid-section and the boat-tail an expansion wave is developed with a marked increase in velocity. As apparent, the velocity field behind the boat-tail portion is very low as compared to the freestream velocity. This wake region, with circulating flow due to the blunt-shaped boat-tail portion of the projectile, generates negative pressure, and is the main contributor of drag in addition to wave, form and skin-friction drags. This is a design constraint and cannot be easily avoided, as the projectile base needs to bear the high pressure generated due to rapidly expanding propellant gases in the firing chamber.

Furthermore, there is a link between the fluctuating flow field at different Mach speeds/orientations and the dynamic behavior of the projectile during flight. An investigation was carried out to derive the correlation of Strouhal number with projectile stability by filtering the dominant frequencies from the lift and yaw force convergence histories. At each time step, the solution is fully converged and the fluctuations are well known to be attributed to vortex shedding and non-symmetric wake behavior, which eventually affects the upstream flow, thereby, disturbing the pressure distribution on the projectile surface.

4.2 Vortex core visualization

To study the opposing flow-field interaction at AoA > 0 deg, the vortex core was plotted with Q-Criterion at Mach 0.7 at 5 degs AoA with 500 and 750 rad/s spin rates, respectively. Q-Criterion is one of the best ways to visualise the turbulent vortical structures, which uses the second invariant of the velocity gradient tensor. Once freestream velocity interacts with surface attached flow swirling with the wall, vortices with circular or spiral set of streamlines are generated. The vortex core with the definition area selected as the projectile is plotted with velocity magnitude variation, which shows the isosurface of vorticity vector on the surface. As evident, the vortex core has increased thickness on +Z-axis face of the projectile where the flow opposes the freestream flow (Figs. 13 and 14) as compared to -Z-axis view where the flow is aligned. This one-sided, wall-attached swirling flow can be observed with the cross-sectional view (at X 0.65 m) with increased thickness of the core, as shown in Fig. 15. The swirling flow, due to flow interaction, will result in surface pressure and shear stress

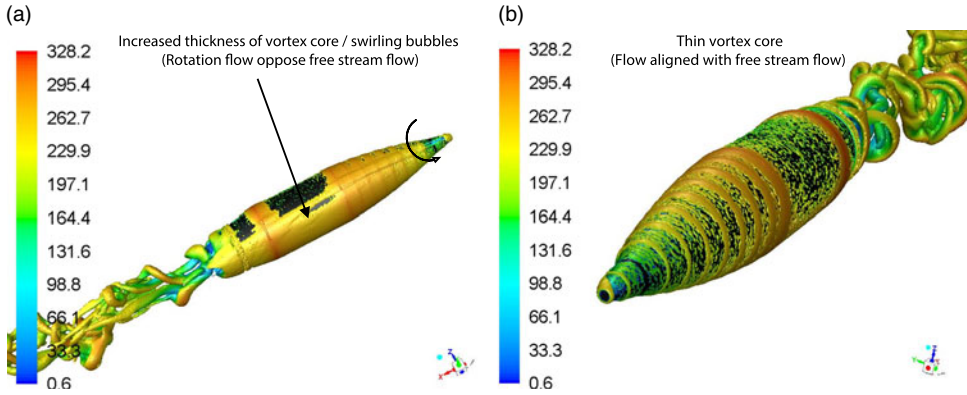


Figure 13. Vortex core (Q-criterion) at M 0.7, AOA 5 degs at 500 rad/s spin rate at T 0.026 sec. a) + Z Axis, b) - Z Axis View.

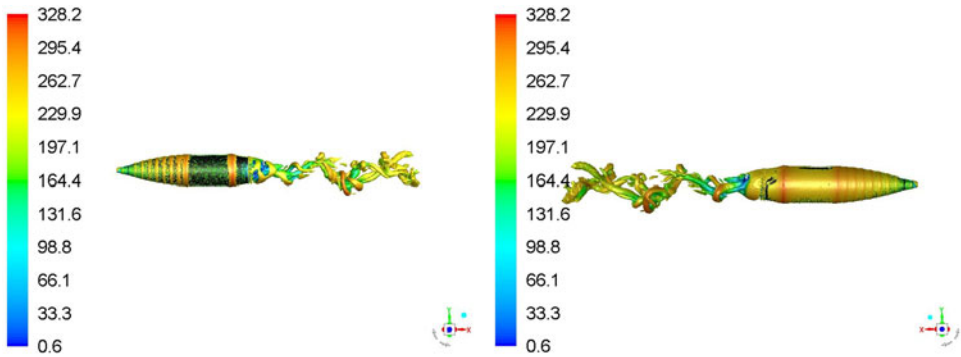


Figure 14. Vortex core (Q-criterion) at M 0.7, AOA 5 degs at 750 rad/s spin rate at T 0.026 sec.

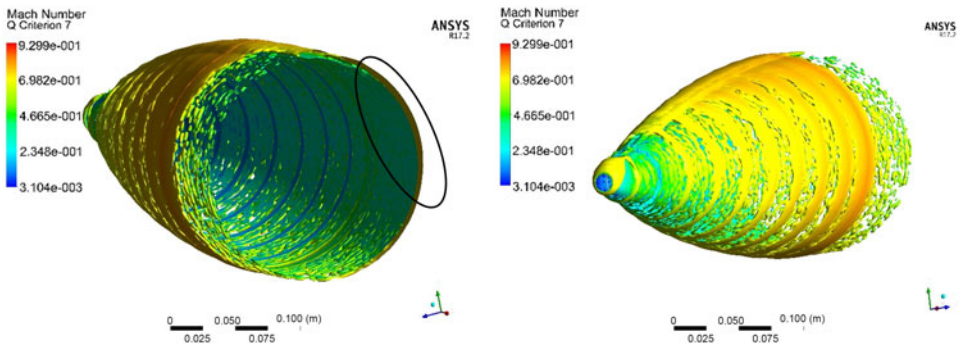


Figure 15. Cross-sectional view of core thickness at (X = 0.65 m from nose) at M 0.7, AOA 5 degs at 500 rad/s at T 0.028 sec.

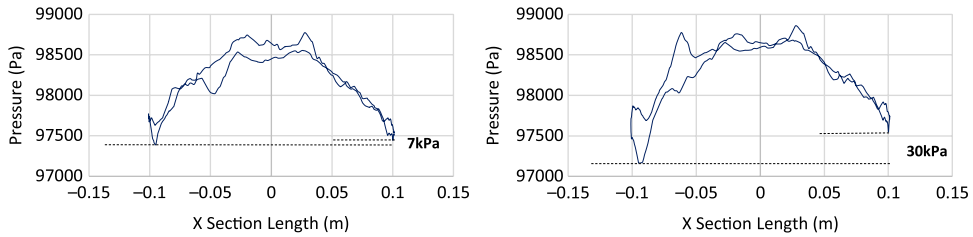


Figure 16. Surface pressure plot at X Sec 0.65 m from nose at M 0.7, AOA 5 degs at 500 rad/s (left) & 750 rad/s (right).

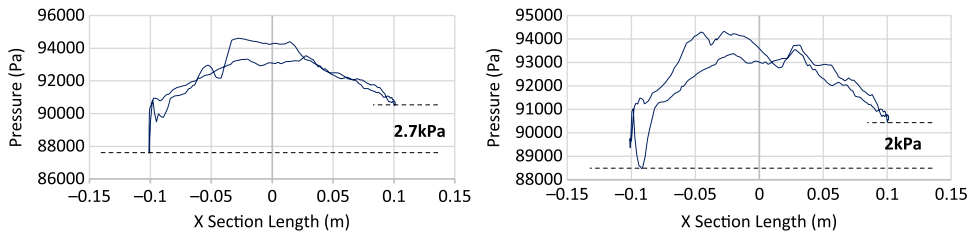


Figure 17. Surface pressure plot at M 1.05, AOA 5 degs at 500 rad/s (left) & 750 rad/s (right).

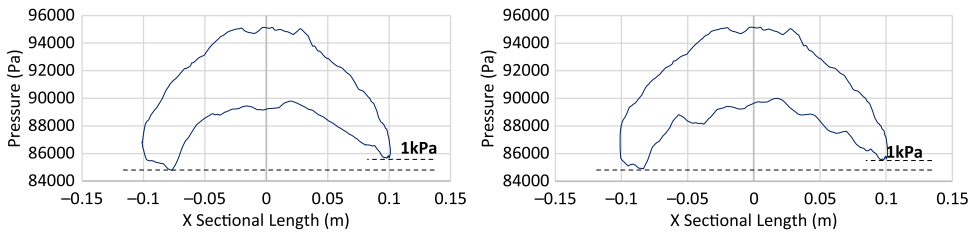


Figure 18. Surface pressure plot at M 1.6, AOA 5 degs at 500 rad/s (left) & 750 rad/s (right).

differential resulting in generation of a Magnus force. It is a function of spin rate, AoA and Mach speed and results in variation of the Magnus force, and moment coefficient at subsonic, transonic and supersonic flow (discussed later in coefficient extraction section).

4.3 Magnus-induced cross-sectional pressure variation

To further understand the effect of swirling flow/ripples development due to Magnus effect, surface pressure was plotted at projectile cross section ($x = 0.65$ m) with different Mach speed and spin rates, as shown in Figs. 16, 17 and 18, respectively. With increasing speed, the pressure differential also increases in conjunction with the increase in AoA and spin rate. The area under the curve analogy shows that the left portion of projectile (as viewed from nose) encounters greater surface pressure as compared to the other half. However, the difference in peak pressure across the projectile increases with spin rate at subsonic speed, whereas it remains negligible at transonic and supersonic speeds. Furthermore, at transonic speed, sudden spikes in the pressure curve are also observed, probably because of the isolated-flow separation bubbles generated due to opposing flows. At transonic speed, Magnus forces and moment coefficient shows inverse behavior as compared to subsonic and supersonic flows behavior, as evident from the coefficient plots.

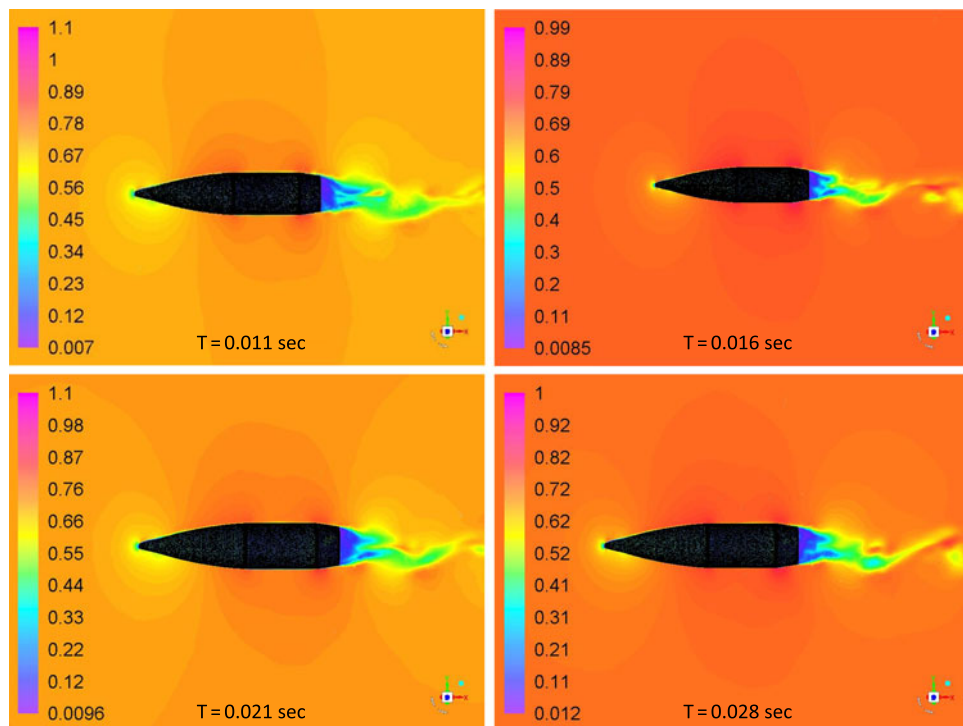


Figure 19. Mach contour plot at various time intervals: M 0.7 at 5 degs AOA, 750 rad/sec spin rate.

4.4 Wake flow and pathline visualization with respect to flow time

Fully developed flow at subsonic speed was analysed with Mach contour plot at various time intervals to visualise the wake flapping and vortex shedding. The shedding of vortices has its effects on upstream flow causing a significant fluctuation in lift-coefficient convergence with respect to flow time, as is also evident from the lift-convergence plot in Fig. 12. However, the shedding frequency may not be identical to vortex shedding from the cylindrical body with infinite length, at low Reynolds number, due to superimposed swirling motion caused by projectile spin, geometry edges and orientation of the projectile. Intuitively, spin imparts more inertia to the shedding vortices in addition to velocity distribution on Y and X axis, causing late detachment and subsequently, reduced shedding frequency. Likewise, the pathline plot shows adequate flow wrapping due to no-slip boundary condition and spinning of projectile. The spin also causes the swirling wake flow, as shown in Fig. 19. The pathlines show separation over the main body and boat-tail edges where the local velocity increases due to generation of an expansion wave, as shown in Fig. 20.

4.5 Strouhal number estimation and dependence on aerodynamic loading

Vortex shedding frequencies at different Mach and spin rates were calculated with the analogy of finding maximum frequency component within the oscillation of lift and yaw-force convergence with respect to time. The dominant frequency corresponds to the vortex shedding frequency, particularly at low Mach speed obtained with FFT analysis. At transonic and supersonic speeds, multiple dominant frequencies were observed, which corresponds to

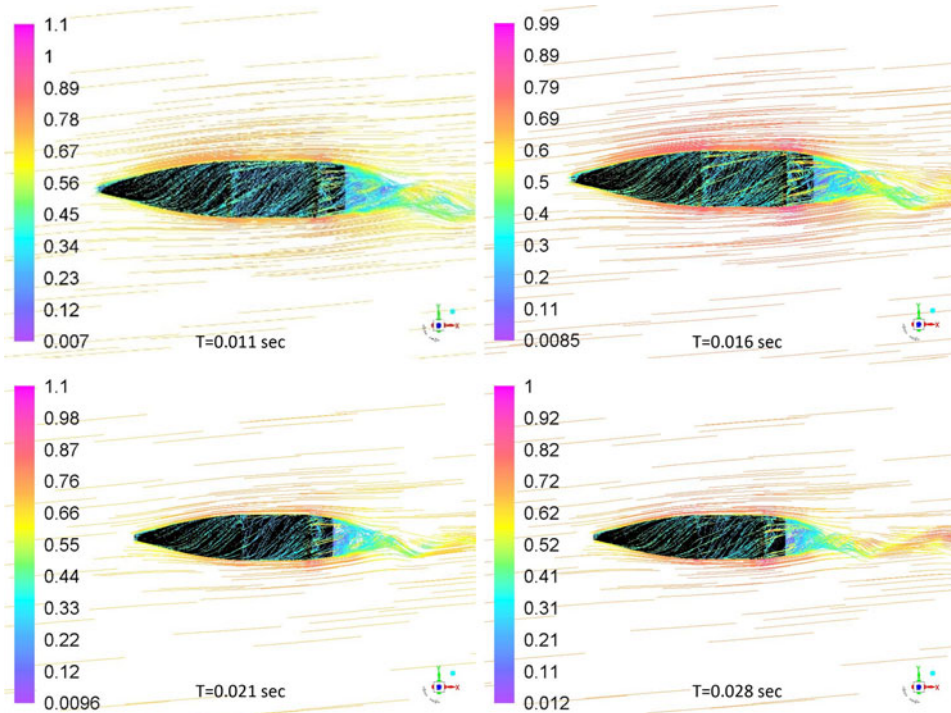


Figure 20. Pathlines Mach plot at various time intervals: M 0.7 at 5 degs AOA, 750 rad/sec spin rate.

multiple vortex shedding as evident from the flow visualization. It is found that both AoA and Mach speed have a direct effect on vortices generation and subsequent variation in lift. The FFT analysis of lift and side forces fluctuation with respect to time at Mach 0.7 is shown in Figs. 21 and 22, respectively.

The Strouhal number, $St(\frac{D}{V})$ calculated from the lift coefficient fluctuation history (considering the dominant frequency only) directly increases with the increase in projectile AoA at 500 rad/s however as the spin rate increases to 750 rad/s, the St shows inverse behavior. Whereas, for side-force coefficient analysis, the Strouhal number increases with the increase in spin rate at low AoA and decreases at higher AoA. The phenomenon can be explained with the help of the FFT plots, in which at higher AoA, multiple dominant frequencies were observed, as depicted in Figs. 21 and 22, respectively. The presence of multiple frequencies corresponds to multiple vortices. At higher AoA, leading-edge separation bubble interaction with trailing-edge vortices shedding, flow encountering large cross sectional area, coupled with swirling action due to spin, leads to generation of complex flow (Fig. 23), as evident from FFT analysis as well. Furthermore, the Strouhal number behavior for side force coefficient differs from lift force at higher AoA/spin rate, and may be attributed to Magnus force effect (results tabulated in Table 3). As depicted in Figs. 13 and 14, the vortex core bubbles appear due to Magnus force with opposite flow interaction and corresponding pressure differential leading to generation of side force. As the Magnus force increases with the increase in AoA, the unsymmetrical flow develops in interaction with the free stream flow leading to generation of turbulence. Hence, Strouhal number shows different behavior for side force as compared to lift-force coefficient.

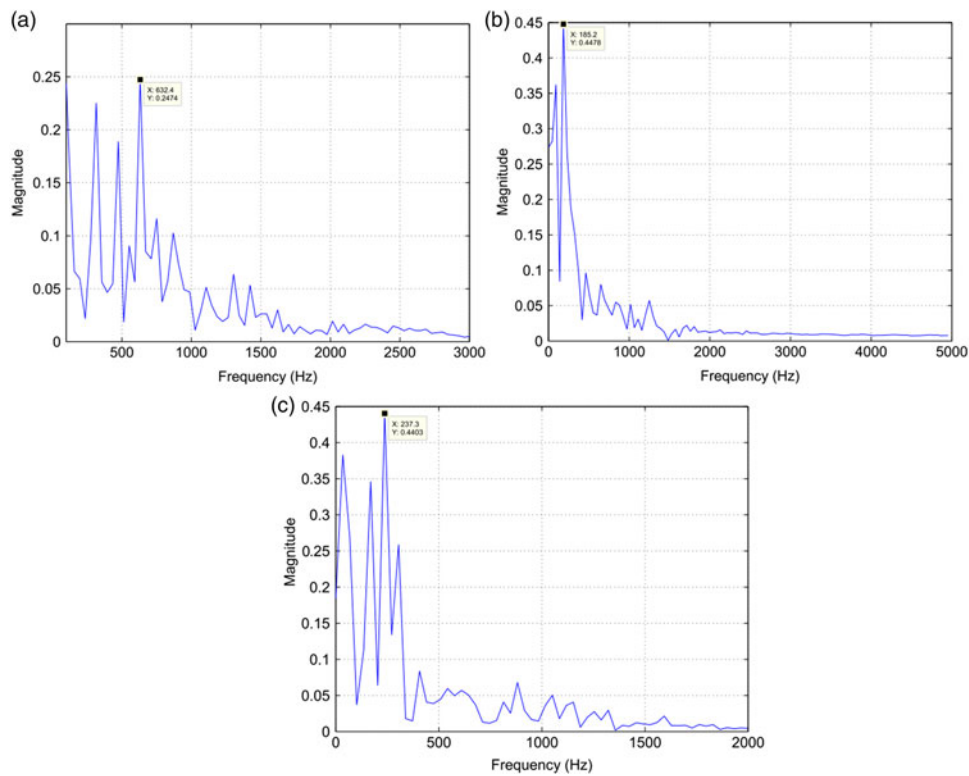


Figure 21. Lift Coefficient convergence FFT plot; M 0.7 AOA, 750 rad/sec spin rate. a) AoA 0 deg. b) AoA 5 degs. c) AoA 10 degs.

4.6 Static/Dynamic coefficient extraction for 6 DoF trajectory analysis

The aerodynamic coefficient library is calculated for generation of in-flight aerodynamic forces and moment for 6-DOF trajectory solver. In the previous study⁽¹⁶⁾, the coefficients were calculated with steady-state analysis and have produced reasonably accurate results when imbedded in 6-DOF motion solver, and the simulated trajectory results were compared with the experimental data. However, the Magnus force and moment coefficient effects were not incorporated and therefore their exits a need to analyse their effect on the trajectory and dynamic stability. Hence, a time-dependent numerical analysis of projectile under study is analysed for Mach 0.7 to 1.6 for 0, 5 and 10 degs AoA, each at spin rate of 500 and 750 rad/sec. Curve-fitting methodology is then used to populate the results for further use in a 6-DOF solver. The calculated coefficients are plotted below from Figs. 24–27.

The steady and dynamic longitudinal/lateral directional coefficients computed were found to have strong dependence on AoA (α) and sideslip angle (β) with respect to Mach speed as the changing parameter. The static coefficients remained in agreement with the steady-state analysis results with reasonable accuracy. However, the dynamic derivatives extracted from transient simulations show variation in Magnus force ($C_{Y\rho}$), Magnus moment ($C_{N\rho}$) and roll-damping ($C_{l\rho}$) coefficients. At transonic speed, the dynamic derivatives show abrupt, varying behavior as compared to subsonic and supersonic speed results. The same trend of Magnus force coefficient variation at transonic speed has been observed in experimental testing of

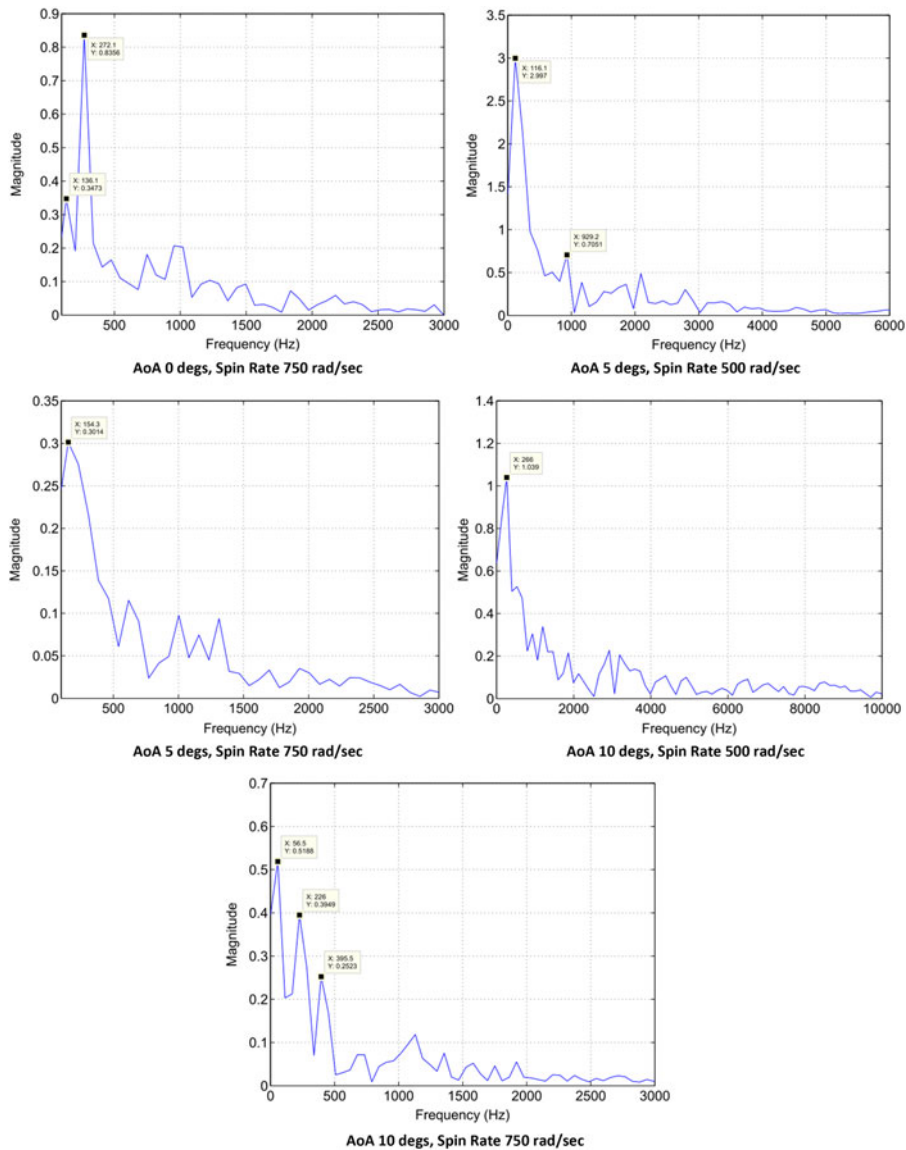


Figure 22. Side force coefficient convergence FFT plots at M 0.7.

8-inch M650 spinning projectile conducted by U.S. Army Ballistic Research Laboratory for incorporation of Magnus force in modified point-mass trajectory model⁽⁷⁾.

5.0 SIMULATED TRAJECTORY RESULTS

5.1 Trajectory validation with experimental results

As for the steady-state analysis, the trajectory simulated results, based on unsteady numerical calculation of aerodynamic coefficients, are found to be in agreement with the experimental

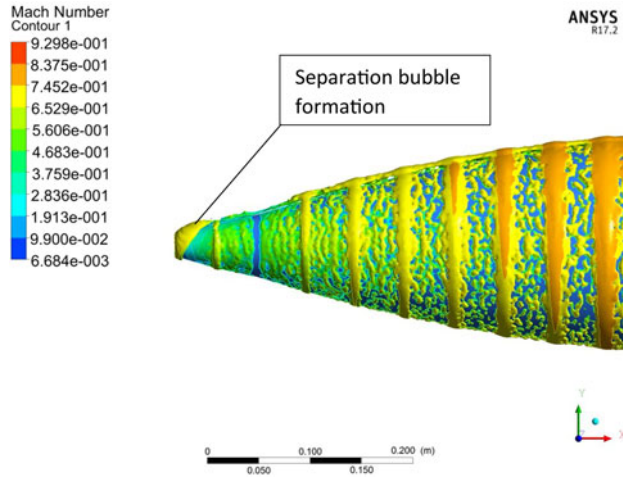


Figure 23. Leading-edge separation bubble and Magnus force induce ripples at M 0.7, AoA 10 degs at 750 rad/sec.

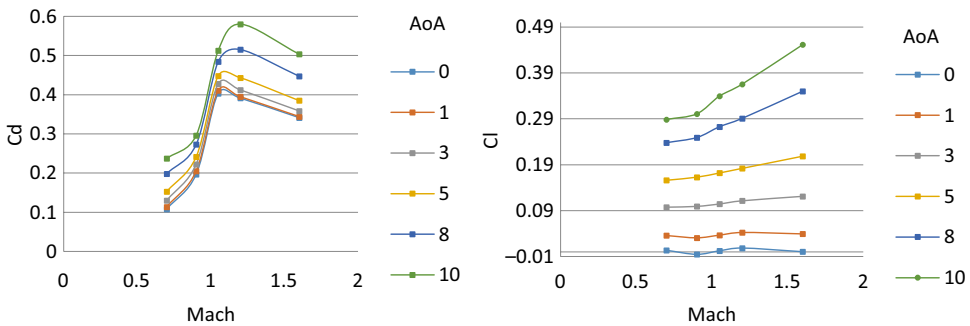


Figure 24. Drag coefficient w.r.t. AoA α (Left) – lift coefficient w.r.t. AoA α (right) at Mach 0.7 – 1.6.

data/firing-table results. However, due to incorporation of Magnus force/moment and time-dependent effects, variation is observed in the dynamic stability of the projectile, particularly at higher Mach speed and AoA. The 6-DOF nonlinear projectile trajectory prediction mathematical model, based on flat-Earth equation of motion, is the same as used by the authors' in the previous study^(16,21). After incorporating the revised dynamic coefficients library (as graphically depicted in Figs. 24–27 above) in 6-DOF trajectory solver, the computed flight parameters were calculated, as plotted from Figs. 28–31.

At Charge 7, the amplitude of oscillations of resultant aerodynamic angle and equilibrium yaw is much higher as compared to low-speed flight at Charge 4. This effect is due to incorporation of Magnus effect in trajectory model that generated side force/moment, thereby, affecting the trajectory with respect to varying AoA and Mach speed. Since the force is a function of speed as well, at Charge 4, the oscillation effect is minimum. As the projectile suffers from continuously acting yaw of repose or equilibrium yaw, generated due to interaction of high gyroscopic effects and gravitational force, the Magnus forces and moments will be produced not only with changing AoA (α), but also due to sideslip angle AoS (β).

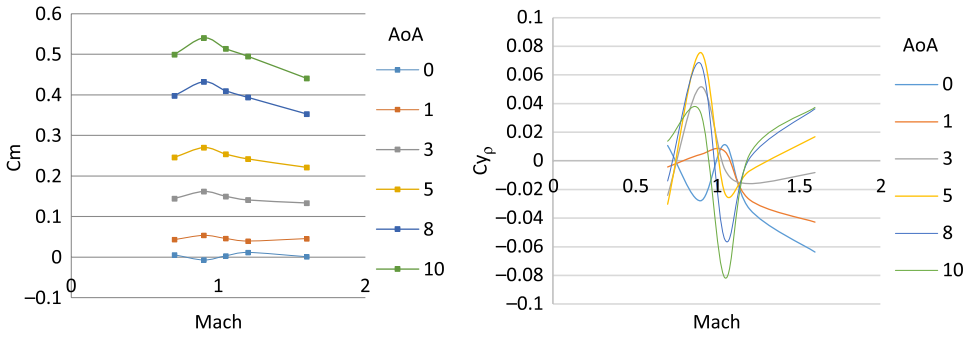


Figure 25. Pitching moment coefficient w.r.t. AOA α (left) – Magnus force coefficient w.r.t. AOA α (right) at Mach 0.7 – 1.6.

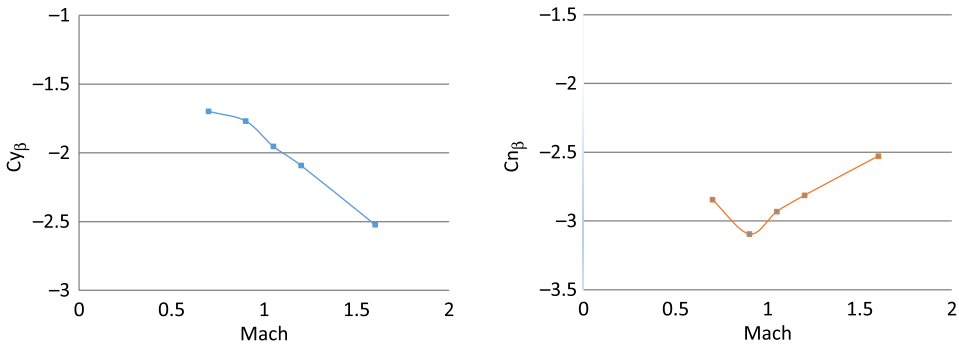


Figure 26. Side force due to sideslip angle (left) - yaw stiffness (right) at Mach 0.7 – 1.6.

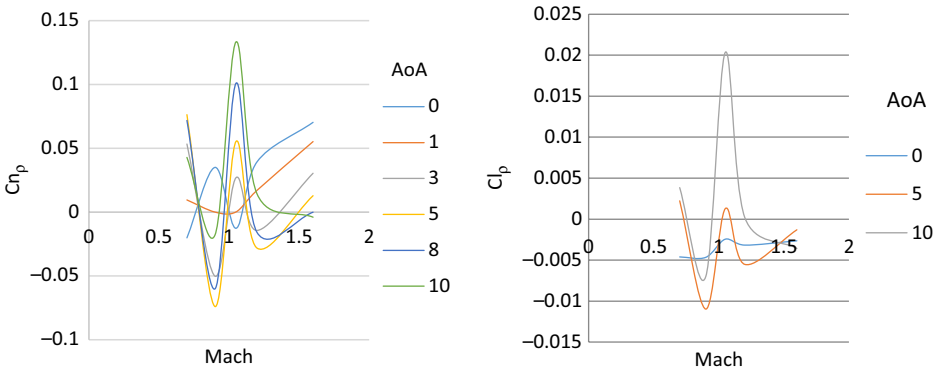


Figure 27. Magnus moment coefficient (left) - roll damping coefficient (right) at Mach 0.7 – 1.6.

Hence, the precession and nutation oscillation effects are magnified as depicted graphically in resultant aerodynamics angle and equilibrium yaw plots (Figs. 29 and 30).

Furthermore, Mach versus range plot at Charge 7 reveals that once the projectile reached apogee, the speed was reduced to the transonic region and the effect of the Magnus force

Table 3
Strouhal Number (St) at Mach 0.7

AoA(deg)	Spin Rate (ρ) rad/sec			
	Cl		Cs	
	500	750	500	750
0	0.1562	0.548	0.1041	0.23616
5	0.2014	0.1606	0.10071	0.1337
10	0.2309	0.205	0.1962	0.04862

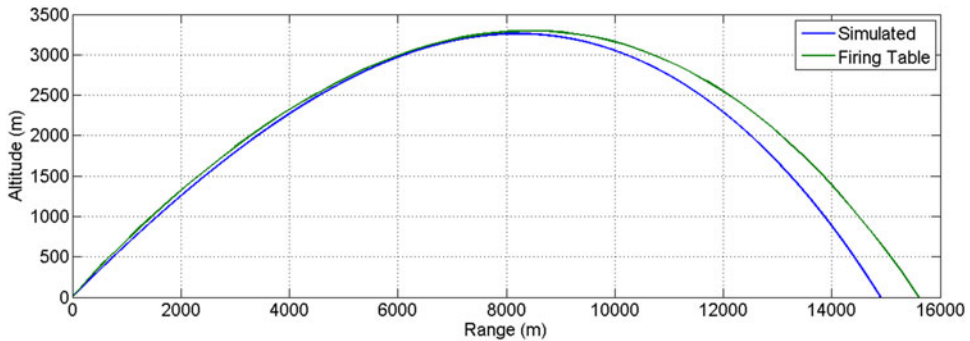


Figure 28. Trajectory plot at charge 7 (MV 595 m/sec) at 600 mils.

varies as shown in the $C_{n\rho}$ and $C_{y\rho}$ plots, respectively. As a result, the oscillation increases at apogee, as is evident from the resultant aerodynamics angle and equilibrium yaw plots. The change in Magnus force as speed increases to transonic may be attributed to fluctuating wake effect and generation of corresponding vortices and their interaction with leading-edge separation bubbles, the trailing-edge vortices and spin-induced swirling flow in the wake region. The generation of a shock wave at transonic speed changes the flow dynamics with velocity and pressure variation behind the shock generation, and subsequently shows sudden variation in calculated dynamic coefficient. However, the pressure differential remains positive and doesn't change the behavior with respect to speed/AoA as depicted in Figs. 16–18.

5.2 Internal dynamics and stability analysis

From classical aeroballistics theory, a spinning projectile executes two types of motions: precession and nutation⁽¹⁸⁾. Precession is the low-frequency oscillation of the angular velocity vector about intended CG trajectory, whereas nutation is the high-frequency circular movement of the body axis around the velocity vector. The frequencies of the two motions corresponds to the two dominant resonance frequencies on the frequency spectral plot of aerodynamic angular motion of projectile in body-axis frame. The FFT analysis of resultant aerodynamic angle with respect to time for Mach speeds 0.7, 1.05 and 1.7 (Fig. 29) revealed specific trends in precession and nutation frequencies. The low-frequency first

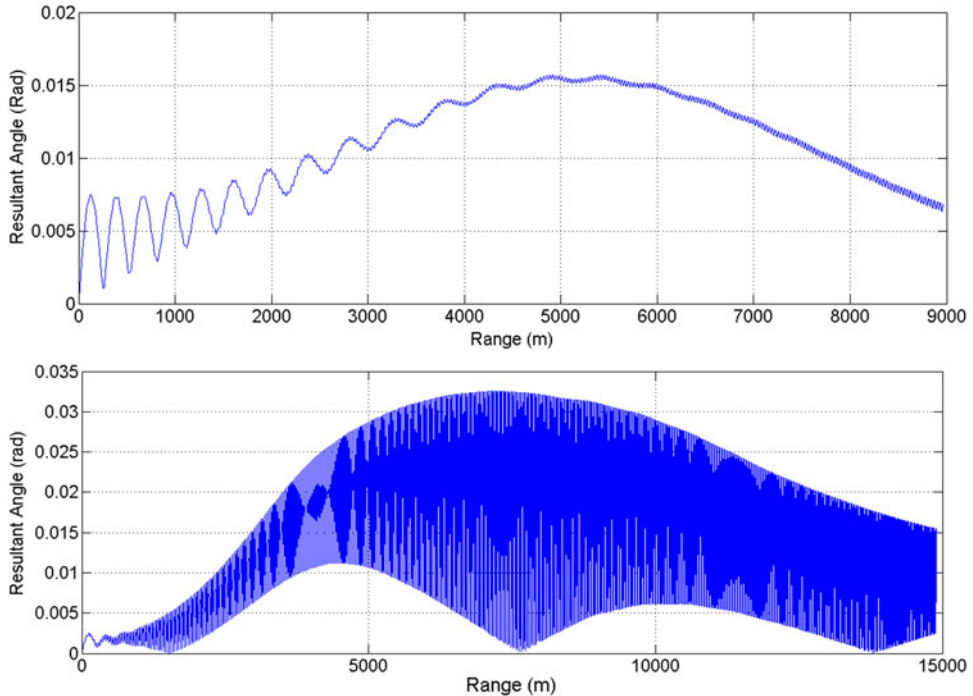


Figure 29. Resultant aerodynamic angle (rad) vs range, charge 4 (MV 350 m/sec) (above) - charge 7 (MV 595 m/sec) (below) at 600 mils.

peak corresponds to precession frequencies, whereas the high-frequency second peak shows nutation frequencies (Fig. 32). As the Mach increases, so do the nutation and precession frequencies for each case. However, as compared to Charge 1 and 4, the precession and nutation frequencies for Charge 7 increase manifolds. This effect is because in descend phase after apogee, the Mach drops to transonic speed, as shown in Fig. 31, at which Magnus force and moment coefficient plots show gradient shift in results.

6.0 CONCLUSION

Magnus force is intrinsic to spinning bodies and significantly affects the dynamic stability and accuracy of bullets/projectiles. However, to capture the Magnus-induced accurately requires time-accurate numerical analysis. The study showed that LES turbulence modelling accurately predicts the Magnus effects. It is observed that the spin-imparted swirling flow, when interacts with the free stream flow at some positive AoA/AoS, develops a pressure differential, which subsequently generates side force and moment. Since axisymmetric, the Magnus force develops along both axis orientations and contributes in generating instabilities in attitude of flight. The FFT analysis at low Mach speed helped in finding the shedding frequencies and generation of multiple vortices with increasing Mach number. The change in Magnus force and moment in the transonic region also affects the dynamic stability of projectile by

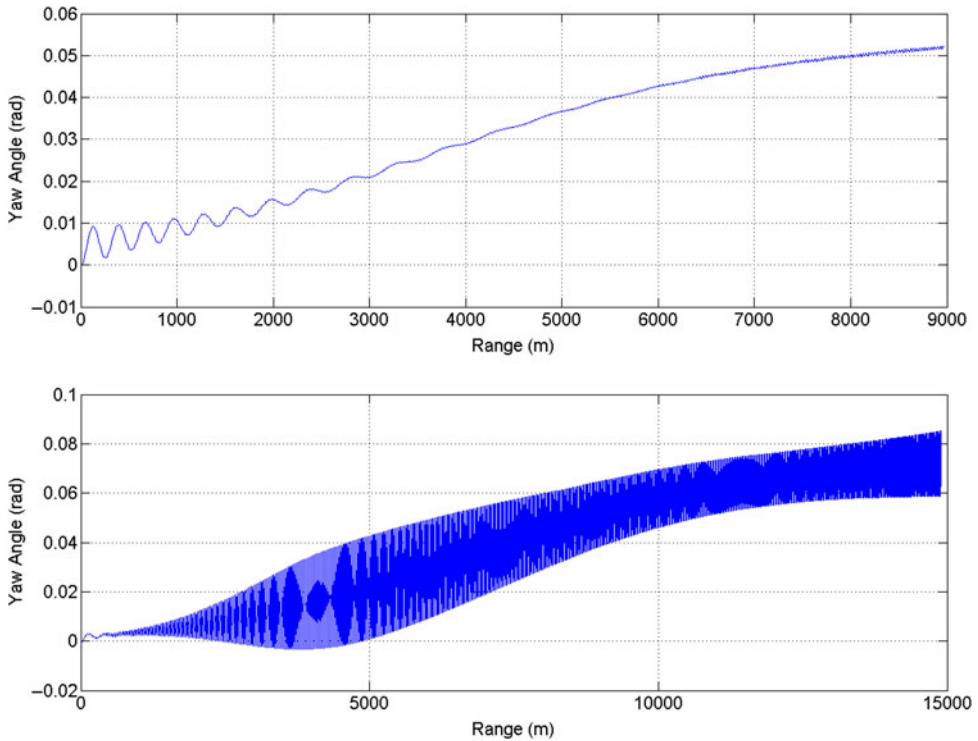


Figure 30. ψ vs range (equilibrium yaw), charge 4 (MV 350 m/sec) (above) - charge 7 (MV 595 m/sec) (below) at 600 mils.

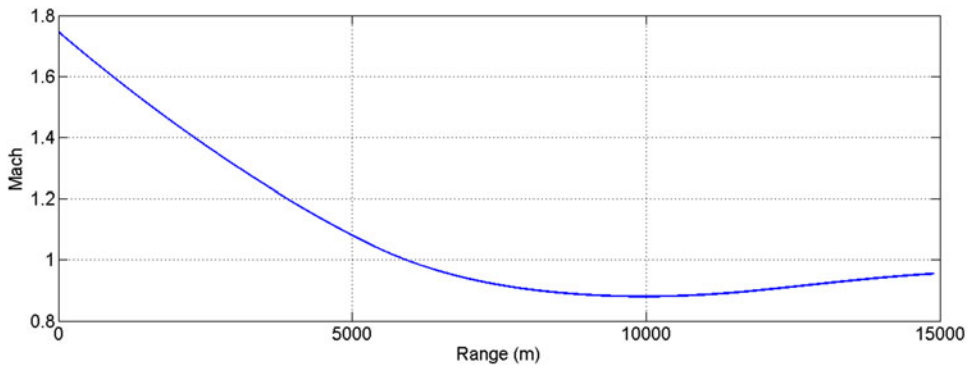


Figure 31. Mach vs range, charge 7 (MV 595 m/sec) at 600 mils.

enhancing the amplitude of oscillation of precession and nutation frequencies, which subsequently affects the accuracy and stability of the projectile. The research may further be extended to analyse the effect of Magnus-induced instabilities on design/CG variation to find optimal, stable flight configuration.

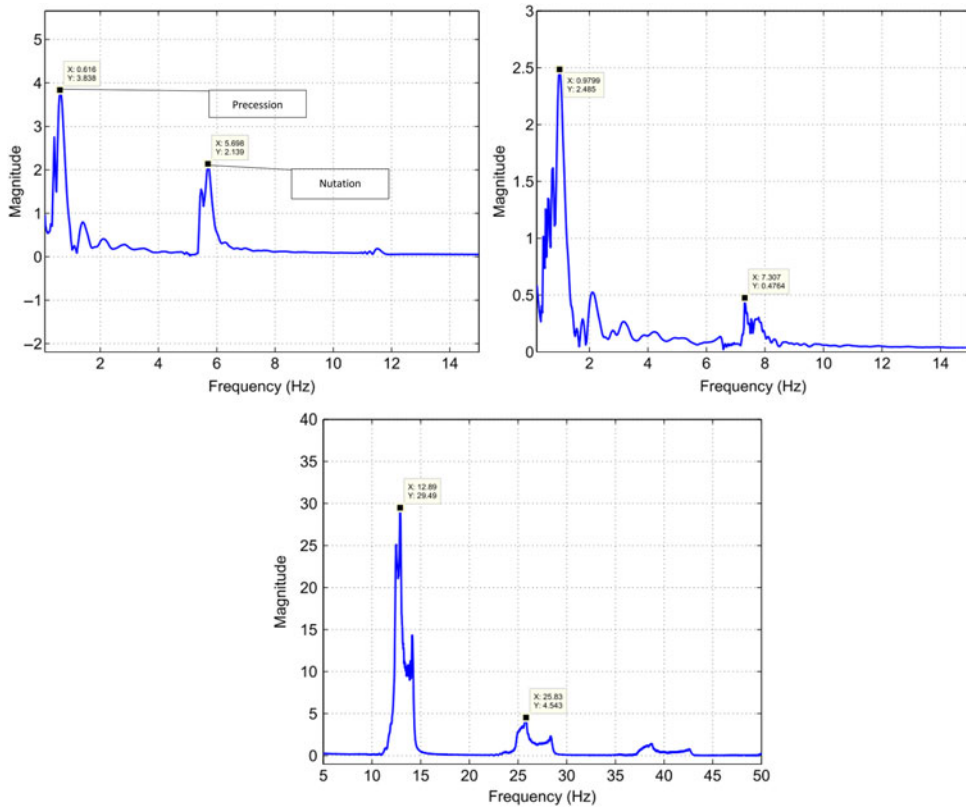


Figure 32. FFT plot charge 1 (MV 249 m/sec) (Left) - charge 4 (MV 350 m/sec) (right) - charge 7 (MV 595 m/sec) (below) at 600 mils.

CONFLICT OF INTEREST STATEMENT

The author(s) declared no potential conflicts of interest with respect to research, authorship, and/or publication of this article.

FUNDING

The author(s) received no financial support for the research, authorship, and/or publication of this article.

ACKNOWLEDGMENT

The first author gratefully acknowledges co-authors Dr. Jehanzeb and Dr. Suhail for their valuable guidance in completion of this research. I especially thankful to my family for their continuous support.

REFERENCES

1. SILTON, S.I. Navier-stokes predictions of aerodynamic coefficients and dynamic derivatives of a 0.50-cal projectile, 29th AIAA Applied Aerodynamics Conference, Honolulu, Hawaii, 27–30 June 2011.
2. DESPIRITO, J. and HEAVEY, K.R. CFD computation of magnus moment and roll damping moment of a spinning projectile, AIAA Atmospheric Flight Mechanics Conference and Exhibit, Providence, RI, 16–19 August 2004.
3. JEHMEY, C. Wind tunnel test on the static aerodynamics of a spinning 106mm artillery shell model, Technical Report WSRL-0090-TR, 1979, Defense Research Center Salisbury, South Australia.
4. MILLER, M.C. Wind tunnel measurements of the magnus induced surface pressures on a spinning artillery projectile model in the transonic speed regime, CRDEC-TR-86081, 1986, Chemical Research Development and Engineering Center.
5. MURPHY, C.H. Free flight motion of symmetric missiles, AD442757, 1963, Ballistic Research Laboratories.
6. MCCOY, R.L. Aerodynamic and flight dynamic characteristics of the new family of 5.56 mm NATO ammunition, BRL-MR-3476, 1985, US Army Ballistic Research Laboratory.
7. LIESKE, R.S. Use of the magnus force in the modified point mass trajectory model, BRL-MR-3870, 1990, U.S. Army Ballistic Research Laboratory.
8. DICKINSON, E.R. The Zero-Yaw drag coefficient for projectile, 8-Inch: HE, M106, BRLM-1681, 1965, US Army Ballistic Research Laboratory.
9. HITCHCOCK, H.P. Aerodynamic data for spinning projectiles, Report No. 620, 1947, US Army Ballistic Research Laboratory.
10. BARANOWSKI, L. Numerical testing of flight stability of spin-stabilised artillery projectiles, *J Theoretical and Applied Mechanics* 2013, 51, (2), pp 375–385.
11. KHALIL, M., ABDALLA, H. and KAMAL, O. Dispersion analysis for spinning artillery projectile, 13th International Conference on Aerospace Sciences & Aviation Technology, ASAT-13, May 26–28, 2009.
12. SAHU, J. Virtual fly-out simulations of a spinning projectile from subsonic to supersonic speeds, 29th AIAA Applied Aerodynamics Conference, Honolulu, Hawaii, 27–30 June 2011.
13. SAHU, J. Computations of unsteady aerodynamics of a spinning body at transonic speeds, 27th AIAA Applied Aerodynamics Conference, San Antonio, Texas, 22–25 June 2009.
14. KLATT, D., HRUSCHKA, R. and LEOPOLD, F. Investigation of the magnus effect of a generic projectile at Mach 3 up to 16 degrees angle of attack, *J Applied Mechanics*, 2013, 80, 031603. doi: [10.1115/1.4023434](https://doi.org/10.1115/1.4023434).
15. http://en.m.wikipedia.org/wiki/Nuclear_artillery.
16. CHUGHTAI, F.A., MASUD, J. and AKHTAR, S. Aerodynamic data generation and 6 DOF trajectory calculation of a baseline large-caliber spinning projectile, AIAA Atmospheric Flight Mechanics Conference AIAA 2016–0784, San Diego, California, USA, 4–8 January 2016, AIAA SciTech.
17. BELAIDOUNI, H., ZIVKOVIC, S. and SAMARDZIC, M. Numerical simulation in obtaining drag reduction for projectile with base bleed, *Scientific Technical Review*, 2016, 66, (2), pp 36–42. doi: [10.5937/STR1602036B](https://doi.org/10.5937/STR1602036B).
18. CHUGHTAI, F.A., MASUD, J., AKHTAR, S. Effect of Design Modifications on Computed Trajectory of a Large-Caliber Spinning Projectile, AIAA Atmospheric Flight Mechanics Conference AIAA 2016–0785, 4–8 January 2016, San Diego, California, USA, AIAA SciTech.
19. CELIK, I.B., CEHRELI, Z.N. and YAVUZ, I. Index of resolution quality for large eddy simulations, *ASME J Fluids Engineering*, 2005, 127, pp 949–958. doi: [10.1115/1.1990201](https://doi.org/10.1115/1.1990201).
20. SEVE, F., THEODOULIS, S., WERNERT, P., ZASADZINSKI, M., BOUTAYEB, M. Flight Dynamics Modeling of Dual-Spin Guided Projectiles, IEEE Transactions on Aerospace and Electronic Systems, September 10, 2016.
21. WESSAM, M.E. Flow field investigations and aerodynamic characteristics of artillery projectile, International Conference of Electrical, Automation and Mechanical Engineering (EAME 2015).